A liquid cooled, high power, steady state, radio-frequency helicon plasma device: PISCES-RF

Saikat Chakraborty Thakur[a], Michael J. Simmonds[a], Juan F. Caneses[b], Fengjen Chang[a], Russell P. Doerner[a], Richard Goulding[b], Arnold Lumsdaine[b], Juergen Rapp[b] and George R. Tynan[a]

[a] *University of California, San Diego, San Diego, CA, USA*
[b] *Oak Ridge National Laboratory, Oak Ridge, TN, USA*

Radio-frequency (RF) driven helicon plasma sources can produce relatively high-density plasmas ($n \sim 10^{19}$ m^{-3}) at relatively moderate powers (< 2 kW) in argon. However, to produce similar high-density plasmas for fusion relevant gases such as hydrogen, deuterium and helium, much higher RF powers are needed. Helicon devices require an insulating sleeve for the RF to penetrate and produce the high-density plasmas. For very high RF powers, thermal issues of this cylindrical RF transparent window limit the plasma operation timescales. To mitigate this constraint, we have designed, built and tested a novel liquid-cooled RF window which allows steady state operations at high power (up to 20 kW). De-ionized (DI) water, flowing between two concentric cylindrical insulators (that act as the RF transparent window), is used as the coolant. A recirculating chiller maintains the temperature of the DI water. We show that a full azimuthal blanket of DI water does not degrade plasma production. We obtain steady-state, high-density plasmas ($n > 10^{19}$ m^{-3}, T_e ~ 5 eV) using both argon and hydrogen. From calorimetry on the DI water, we measure the net heat that is being removed by the coolant at steady state conditions. Using infra-red (IR) imaging, we calculate the constant plasma heat deposition and measure the final steady state temperature distribution patterns on the inner surface of the ceramic layer. We find that the heat deposition pattern follows the helical shape of the antenna. We also show the consistency between the heat absorbed by the DI water, as measured by calorimetry, and the total heat due to the combined effect of the plasma heating and the absorbed RF. These results are being used to answer critical engineering questions for the 200 kW RF device (MPEX: Materials Plasma Exposure eXperiment) being designed at the Oak Ridge National Laboratory (ORNL) as a next generation plasma material interaction (PMI) device.

1. Introduction

The plasma facing components in the divertor regions of toroidal magnetically confined thermonuclear fusion reactors such as ITER, DEMO or any other future burning plasma devices will face some of the most extreme heat and plasma fluxes known to mankind [please see Ref. 1 and the references within, for a detailed review on this subject]. Understanding and mitigating the unwanted effects of extremely hot plasmas on the plasma facing components is key to the successful and long-lasting operation of future fusion reactors. In this regard, plasma material testing facilities serve a crucial role in thermonuclear fusion research [Ref 2 and the references within]. However, the ability to examine plasma materials interactions (PMI) and the evolution of the plasma-material interface over time due to the high fluences on the divertors is quite difficult in current (or planned) toroidal devices, mostly due to lack of proper diagnostic access and lack of controlled experiments [3, 4]. Linear plasma facilities simulating plasma facing conditions have filled in this gap with the capability to achieve high fluences to serve as PMI testbeds [Section 3 of Ref. 2] with state-of-the-art diagnostic capabilities, easy access and a well-controlled plasma environment.

The standard mechanism of plasma production in most of the linear PMI devices currently in use, that can produce high density plasmas (10^{18} m^{-3} – 10^{19} m^{-3}) in steady state to achieve high fluences, is to use a DC arc plasma generator with a heated lanthanum hexaboride (LaB_6) or tungsten cathode. Please see the Section 3 of Ref. 2 for a comprehensive summary of most of the current linear plasma devices used for PMI studies. Depending on the details of the design of the arc sources, the most commonly used plasma generation techniques are LaB_6 based cylindrical cathode sources [5], or reflex arc sources [6 – 9] compatible with magnetic fields of up to ~ 0.1T and high pressure, pulsed, cascaded arc sources [10, 11], which works better at magnetic fields of ~ 1T. These have been the standard method of producing relatively high-density plasmas for PMI studies over the last few decades. However, the design of these sources require that they are in direct contact with the high-density plasma, which can lead to several additional issues such as introduction of impurities in the plasma, finite lifetime of the cathode and difficulty in reproducibility after a long machine maintenance break.

On the other hand, radio frequency (RF) based plasma sources have been used in the basic plasma physics community for the last few decades to produce similar densities in argon plasma [12 – 15]. Depending on the external magnetic field and power, these RF devices can operate in the capacitive, inductive or the helicon mode. In the helicon mode of operation, RF sources can produce peak plasma densities of at least 10^{19} m^{-3} in argon for a few kW (kilowatts) of RF powers in plasma chambers that are several meters long [16, 17]. Helicon plasma sources have the additional benefit of having the antenna mounted outside of the vacuum

Author's email: saikat@eng.ucsd.edu

chamber which minimizes impurities in the plasma. Moreover, the axial access to the vacuum chamber in the source end of the device is unobstructed by the source itself (unlike the arc discharge sources) and hence can be directly used for diagnostic access and laser heating. Also, RF devices are very repeatable even after long device downtimes. Finally, even if operating the helicon source needs small windows of operation in the magnetic field domain, there is no restriction on the magnetic field in the main plasma chamber housing the target. Thus, these plasma sources can be used in PMI devices if similar densities are achieved in steady state in fusion relevant gases such as deuterium (D), hydrogen (H) or helium (He). However, plasmas with lighter ions have a higher thermal velocity and would need more RF power to sustain similar high densities. Hence, in the past few years, there have been a sustained research endeavor to build RF sources for PMI studies using much higher powers [18 – 22] for use with low mass gases.

RF driven helicon sources require an insulating sleeve for the RF to penetrate and produce the high-density plasmas. For very high RF powers, thermal issues of this cylindrical RF transparent window limit the plasma operation timescales. The current high-power RF sources in operation that are designed for PMI studies are hence all operated in the pulsed mode with the plasma being ON for only up to few hundreds of milliseconds [20, 21]. To increase the net fluence on to the material target that will be compatible to real tokamak discharges, it is desirable to accomplish steady state operations with low mass, high density plasmas. To allow steady state operations, we have to mitigate the thermal constraints, while maintaining the mechanical integrity of the RF source. Hence, we have designed, built and tested a novel liquid-cooled RF window which allows steady state operations at high power (up to 20 kW) with both argon and hydrogen plasmas. De-ionized (DI) water, chosen to minimize RF absorption, flowing between two concentric cylindrical insulators is used as the coolant. A recirculating chiller maintains the temperature of the DI water. The RF transparent window thus effectively comprise of these two ceramic cylinders and the DI-water layer. This is the first example where the RF transparent ceramic layer is fully immersed in a completely azimuthal blanket of a liquid coolant (DI water in this case). This is designed in order to achieve the most uniform cooling possible. In the only other example of a water cooled ceramic for a helicon source, in the experiment RAID [22], cooling channels have been drilled into the ceramic itself, at 8 azimuthal locations, to keep the ceramic relatively cold for plasmas up to 5 kW of RF power. At these powers, hydrogen plasma with densities < 10^{18} m^{-3} were formed. But for steady state operations in PMI relevant high density (> 10^{19} m^{-3}) hydrogen or deuterium plasma, more uniform cooling is required, especially as new PMI devices, such as the Materials Plasma Exposure eXperiment (MPEX) at Oak Ridge National Laboratory (ORNL), are being designed for up to 200 kW of RF power [23, 24]. The design of the DI water cooled RF source assembly described here is motivated by stringent requirements of the MPEX device. The conceptual design and preliminary numerical analysis of the performance of a water-cooled ceramic window for the MPEX device has been mainly based on short pulse thermal data of an uncooled source, currently used in Proto-MPEX [25].

In this paper, we investigate several crucial experimental questions associated with this DI water cooled RF source design. First and foremost was whether the coolant would absorb too much of the RF from the antenna and thus prevent the formation of the high-density helicon mode. We also have to carefully design both a water seal and a vacuum seal within the antenna assembly, using ceramic to metal sealing technology. Would this intricately designed source assembly be mechanically and structurally safe to use at high powers? Will the cooling system work as expected and remove the heat deposited on the ceramic by the plasma in real time to achieve thermally steady state conditions? What are the heat and steady state temperature distributions on the inner plasma facing surface of the ceramic? This is crucial as otherwise the non-uniform heat accumulation on the inner surface of the inner ceramic can cause unequal temperature distributions leading to strong thermal gradients which can cause catastrophic stress fractures of the ceramic. Finally, how does the important engineering parameters scale with RF power? This will help in extrapolating our results to higher powers for future RF devices.

Here, we show that the new DI water cooled RF transparent window design allows us to produce high density, steady state plasmas in both argon and hydrogen. Moreover, the results from this study are being compared to thermal-hydraulic (Computational Fluid Dynamics: CFD) and thermal-structural (Finite Elements: FE) simulations to answer critical engineering questions that arise in designing the 200 kW RF source for the MPEX device at ORNL [26]. Based on the experimental results, we have already provided important feedback on several aspects for necessary upgrades to the MPEX 200 kW RF source assembly design.

2. Experimental set up

2.1 The plasma device

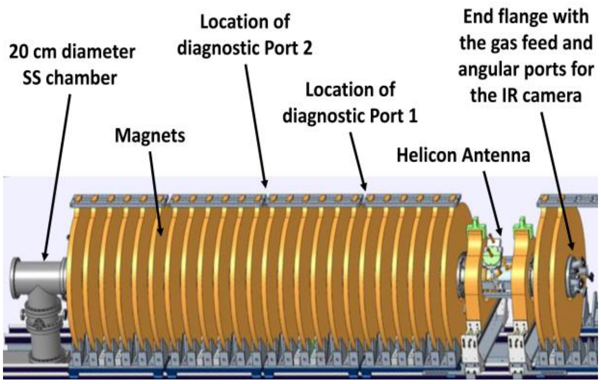

Fig. 1. CAD model of the PISCES-RF device.

Fig. 1 shows the CAD (Computer-Aided Design) model of the experimental device, pointing out some of the important aspects of the experiment. During actual plasma operation, the source assembly (Helicon Antenna area in Fig. 1) is covered with RF shielding to prevent RF noise escaping into the room, which can disrupt or damage sensitive diagnostics. Also, not shown is the matching box that is connected to the leads of the antenna (which are shown as copper rods sticking out at an angle of ~ 45 degrees). The new RF source assembly with the DI water cooled RF transparent window (detailed description is given in the next section 2.2) was incorporated on to an existing linear magnetized plasma chamber, located in the PISCES (Plasma Interaction Surface Component Experimental Station) laboratory at the University of California at San Diego (UCSD). Since the primary goal of this new device would be to produce steady state plasmas at high densities to generate extremely high fluences for PMI studies, we shall henceforth call this machine PISCES-RF.

The main cylindrical plasma chamber, along with the external magnets and pumping system belonged to the erstwhile Controlled Shear Decorrelation eXperiment (CSDX) [17, 27 – 38]. Previously in CSDX, argon plasmas with high density and relatively low temperatures ($n > 10^{19}$ m^{-3}, $T_{electron} \sim 5$ ev and $T_{ion} < 1$ eV [39]) were produced using an m = 1 helicon antenna, operating at 13.56 MHz at RF powers of ~ 1.5 – 2 kW. The plasma device consists of a 3 m long, 20 cm diameter stainless steel (SS) chamber immersed in an external magnetic field that can go up to 2400 Gauss. In this work, the magnetic field used is almost uniform for most of the length of the machine, expect at the location of the helicon source, which has a small ripple due to the extra separation of the two magnetic field coils around the RF antenna. This extra space allowed us to safely install the high-power RF antenna assembly and build a grounded RF shield around it. A turbomolecular pump, placed at the downstream end of the chamber, backed by two other mechanical pumps allows the base pressure to be in the high 10^{-7} Torr. Argon gas, at few milli-Torr(s), was originally fed downstream of the RF source. A manually controlled valve placed near the pumps allow us to change the neutral pressures in the device independently from the gas flow rate. In the current set up, we have added a specially designed end flange (please see Fig. 2 for the details) upstream of the RF source that allows upstream end gas injection. This gas injection configuration has shown to critically affect the neutral gas management in Proto-MPEX [40] and is also the choice of operation for MPEX. Hence, we incorporated this change on PISCES-RF. We currently have the option of using both an upstream or downstream gas injection.

2.2 DI-water cooled RF source assembly

CSDX had a water-cooled RF antenna, but the existing RF transparent window was an air cooled pyrex glass bell jar. Compressed air was sufficient to keep the bell jar cold as CSDX used argon plasmas in the range of 1.5 – 2 kW. To achieve steady-state operation in high density H, D or He plasma, we need to operate at up to 20 kW of RF power and hence the helicon window must be cooled by a chilled liquid coolant. The RF transparent window material requires a low dielectric constant to limit losses. Hence, we chose the inner window to be alumina (Al_2O_3), having a thickness of ~ 6.35 mm (0.25 inches), while the outer window is quartz with thickness of ~ 3 mm (0.117 inches). The annular water channel in between the two ceramics is ~ 3.35 mm (0.133 inches) wide. The inner diameter of the alumina cylinder is ~ 12 cm (4.75 inches). The RF transparent ceramic window assembly has an outer diameter of ~ 14.6 mm (5.75 inches). This assembly is attached to conflat flanges on the two ends so that the whole assembly is compatible to both the CSDX chamber at UCSD and the Proto-MPEX chamber at ORNL.

DI water is used as the coolant to reduce RF absorption by the coolant. We used a recirculating heat exchanger to cool the DI water and re-route it back to the source. Since DI water can be corrosive to copper or brass, we designed the whole recirculating chiller and the corresponding plumbing system using PVC piping and SS adapters. Note that the RF antenna itself is made from copper, and hence the cooling lines for the antenna itself are kept separate from the DI-water coolant lines for the ceramic. Moreover, to reduce impurities in the plasma, a ceramic-to-metal joint is expected to be used in MPEX for the water-to-vacuum boundary. In the experiments shown here, we used a ceramic to metal sealing technology using titanium brazing, assembled for us by MPF Inc. This method is also expected to be used by ORNL to build the RF source assembly for MPEX.

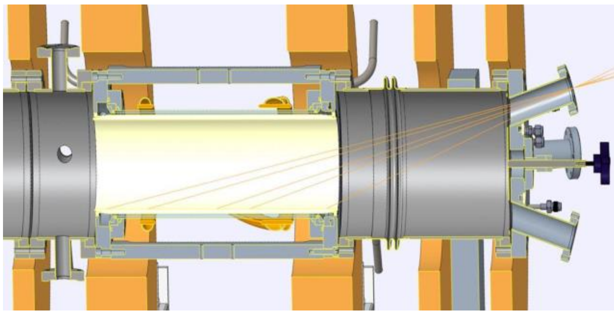

Fig. 2. CAD model showing a cross section of the new DI-water cooled RF source assembly, along with the end flange with the angular viewports for IR imaging of the inner ceramic surface.

In Fig. 2, we show the main aspects of the new source assembly. The SS chambers are shown in dark gray. The external magnets are shown in dark yellow. The ceramic RF transparent window is shown in white, over which the water-cooled helicon antenna (cross section of which is shown in golden) is wrapped. The mechanical supports for the ceramic and the RF antenna assembly is shown in light gray. The DI water is introduced in between the two concentric ceramic layers through bores drilled into the end SS flanges, at 4 symmetrically placed azimuthal locations. The gray SS tubes bent upwards from the two end flanges are the inlet and outlet channels of the DI water. The upstream end flange, shown towards the right side of the image in Fig.

2 has been specially designed with four angular ports for infrared (IR) camera access to get a full azimuthal view of the inner ceramic surface. The yellow straight lines originating at the center of one of the angular ports show that the whole axial length of the inner ceramic surface is accessible to the IR camera view. This allows us to produce full z – θ maps of the plasma heat deposition and final steady state temperatures. The end flange is also fitted with ultra-high vacuum compatible valves for end gas injection. We also have a water-cooled end plate, which acts as a shutter for the IR windows when the IR camera is not being used and also as an upstream dump plate for the plasma.

3. Diagnostics

In an RF source, we need a matching network for efficient coupling of the RF power from the power supply to the antenna. One of the biggest challenges in this design was to ensure that the presence of the coolant should not absorb too much of the RF so as to hinder high-density plasma production. We used a Vector Network Analyzer (VNA) to measure the RF losses due to the DI water coolant, by measuring the return loss of the RF matching circuit when attached to the antenna with and without the coolant in between the two ceramic layers. The return loss, which is given by

$$Return\ Loss\,[\text{dB}] = 10\,.log_{10}(P_{reflected}/P_{forward}), \quad (1)$$

is measured as a function of the input frequency in the absence of plasma. At the resonant condition, the reflection is minimum, indicating maximum absorption of RF power by the loaded resonant circuit. The quality factor (Q_L) of a loaded resonant circuit is related to the width (Δf) of the return loss curve, which in turn is related to the vacuum resistance (R_v), by the equation

$$Q_L = f_0/\Delta f = (\omega_0 L)/(2R_v). \quad (2)$$

Here f_0 is the resonant frequency, ω_0 is the angular frequency at resonance and L is the inductance of the RF antenna. The width of the return loss curve can be calculated from the values of the input frequencies at the 3 dB points and the corresponding vacuum resistance, R_v, is given by

$$R_v = \pi L \Delta f. \quad (3)$$

Thus, by measuring the 3-dB width of the return loss curve using the VNA, with and without the coolant, we can calculate the difference in the RF loading, which gives an estimate of the RF losses due to the coolant.

To measure the RF losses in the presence of plasma, we used a Pearson transformer to directly measure the current through the antenna and along with the measured forward power to the RF antenna, we can calculate the effective resistive loading. Again, we perform these experiments with and without the coolant to measure the difference in the resistive plasma loading. This method can also be used to measure the resistive vacuum loading.

To measure the temperature of the plasma facing inner surface of the ceramic (alumina), we used an FLIR T420 camera operating at 30 Hz, with a spatial resolution of 240 x 320 pixels for infrared (IR) imaging. Due to mechanical constraints, the IR camera was placed at a shallow angle, as shown in Fig. 2 (the line to the center of the ceramic is ~ 17° with respect to the horizontal plane). This ensured that the IR view encompasses the full axial range of the inner surface of the ceramic. Four such symmetrically placed angular ports allowed us to obtain a full azimuthal view of the inner ceramic surface. From the IR camera location, the cylindrical ceramic surface looked like a part of a truncated cone, which was then mathematically mapped to a z – θ plane. Each individual azimuthal position of the IR camera recorded a little more than ± 90° azimuthal view of the inner surface of the cylindrical ceramic. With IR imaging data from four such locations, we mathematically reconstructed the full z – θ thermal maps of the cylindrical surface. We also found that the shallow angle of the viewport allowed the IR emission from the uncooled, hot chamber walls to reflect off the polished white ceramic surface back onto the IR camera. This gave a spurious contribution to the IR data, which had to be corrected for. We performed calibration by cooling the chamber walls using liquid nitrogen. The mathematical mapping algorithms and the methods used to take care of the spurious IR reflection, that could otherwise lead to erroneous interpretation, are being presented elsewhere [41].

We also used two thermocouples to measure the inlet and the outlet temperatures of the coolant DI-water, as a function of time. From the difference of these measurements, we could use calorimetry to calculate the net amount of heat that was being removed by the coolant. This also gave us the timescales of how fast the system reached steady state. This information turned out to be an important parameter in understanding and determining the steady state temperature from the IR camera analysis, that allowed us to get rid of the spurious contribution from the back reflection of the hot chamber during IR imaging.

Finally, we used two RF-compensated, voltage-swept Langmuir probes to measure the standard plasma parameters such as the plasma density, electron temperature, floating and plasma potentials at two axial locations, 0.8 m and 1.5 m downstream of the RF antenna.

4. Experimental Results

4.1 Effect of DI water on RF absorption and high-density plasma production

The foremost concern regarding this liquid cooled RF antenna design was the fact that there is a fully azimuthal blanket of liquid under the RF antenna. This section explores the effect this has on RF absorption and high-density plasma production. We will show that we can produce high density plasma with this RF source design.

As explained in section 3, we used the VNA to measure the return loss of the matching circuit, loaded by the RF antenna, both with and without the DI water coolant. In Fig. 3, one example of such a return loss measurement is shown. Red circles are data with the coolant flowing, while the black squares are without any coolant in between the two ceramics, and this same scheme is used for Fig.(s) 3 – 7. From the return loss curves shown in Fig. 3, we calculated the widths using the upper and lower frequencies at the 3-dB cut off points and used the resonance frequency and equations (2) and (3) to calculate the quality factor (Q_L) and the vacuum resistance (R_v). In this particular case, when we do not have the DI water coolant in the RF source, Q_L = 125 and R_v = 0.164 Ω. When we introduce the DI water coolant in the RF source, we get Q_L = 112 and R_v = 0.184 Ω. Thus, the effect of introducing the DI water was a reduction of the quality factor by 11% and increase in the vacuum loading resistance by ~ 0.02 Ω, which is not very concerning. For many scans over multiple days, this factor ranged from 7% to 11%. We also notice that the resonance frequency shifts by ~ 0.08 MHz. This is expected, as introduction of the DI water coolant slightly changes the impedance of the RF antenna assembly. But this small change in the resonance frequency could be easily taken care of by the tuning capacitors in the matching circuit.

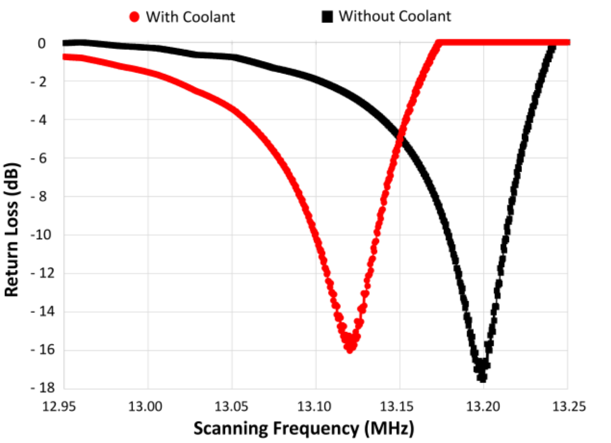

Fig. 3. Return loss, measured using a VNA, showing the RF absorption with and without the coolant (DI water) in the source.

In Fig(s). 4 and 5, we show the results of RF loading measurements using the Pearson transformer in the cases with no plasma (RF power was turned on, but the neutral gas was not injected) and with plasma operation, respectively. For each chosen RF power input, we measured the corresponding current through the leads of the RF antenna and calculated the resistive leading. We show the normalized resistive loading with and without the DI water coolant. We found that the effect of introducing the DI water coolant was to effectively increase the resistive loading, which is consistent with what we found using the VNA. For vacuum conditions, the increase in the loading by 5% to 9% of the original antenna loading (without the DI water coolant).

When the plasma is turned on, as in most typical RF driven helicon sources, we find several mode-jumps from the Capacitively Coupled Plasma (CCP) to Inductively Coupled Plasma (ICP) and finally the helicon mode. Even though these differential measurements can introduce a lot of uncertainty (as we are taking a small difference between two large numbers), we can observe the effect of these mode jumps on the resistive loading of the matching circuit. They are consistent with the typical visual characteristics of mode jumps in similar helicon devices [16, 17]. More importantly, we can clearly see the effect of the DI water coolant on the resistive loading. In our regime of interest (high power helicon mode of operation), it seems that the effect of DI water coolant on the loading is to increase it by 9 ± 1 %. Since this experiment required operating the source without the DI water coolant, we did not operate the machine with higher than 3 kW of RF power, for safety issues.

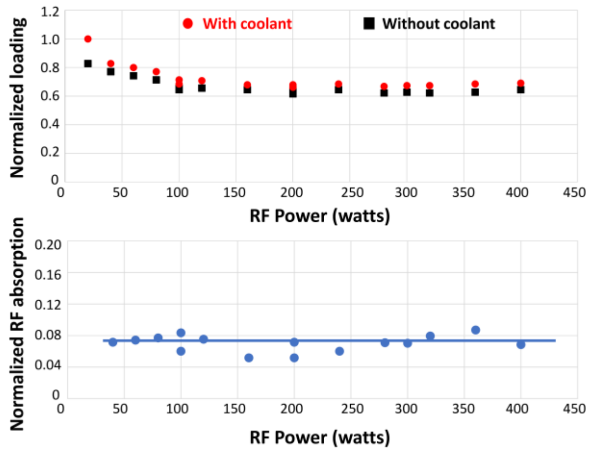

Fig. 4. Normalized loading with and without the DI water coolant in the source, and the corresponding RF absorption. The multiple points plotted for 100 W and 200 W are taken on two different days to show reproducibility.

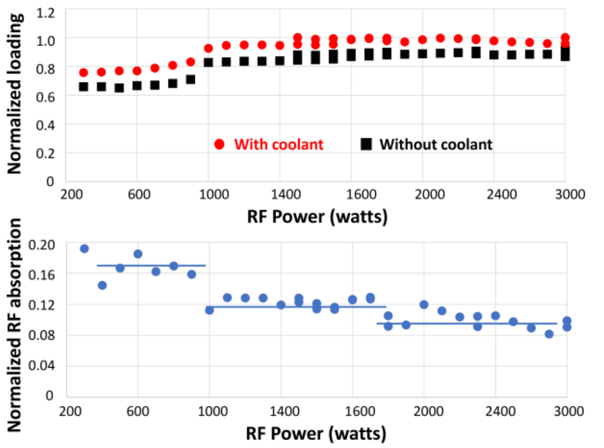

Fig. 5. Normalized loading with and without the coolant (DI water) in the source, and the corresponding RF absorption during plasma operation. The multiple points plotted for the same RF powers represent data taken on different days.

As a final test of whether the DI water coolant affects high density plasma production, we show the radial profiles of the plasma density and the electron temperature with and without the DI water coolant, as measured by the RF compensated, voltage swept Langmuir probe in Fig(s). 6 and 7 respectively. These measurements were obtained ~ 0.8 m downstream of the RF antenna, in argon plasma. For only 2 kW of RF power, with ~ 4 mTorr of neutral argon gas flowing at 50 sccm and with uniform magnetic field of 950 G, we achieve a peak electron density ~ 1.95 x 10^{19} m^{-3}. We find that the effect of the DI water coolant in the RF source on plasma production is negligible. The very slight differences can probably be attributed to the different matching conditions in the two cases, as also found in the VNA results. Introduction of the DI water coolant changes the effective RF antenna impedance and hence can shift the resonance matching conditions. However, it is clear that the presence of the DI water coolant does not hinder high density plasma production.

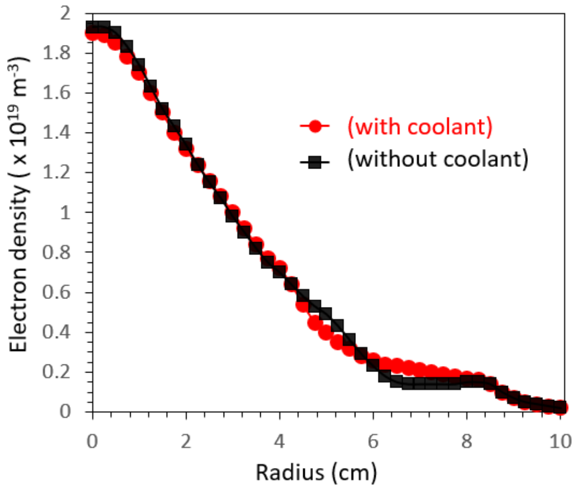

Fig. 6. Plasma density (at 4 kW in argon) with and without the DI water coolant in the source. The shots are very repeatable.

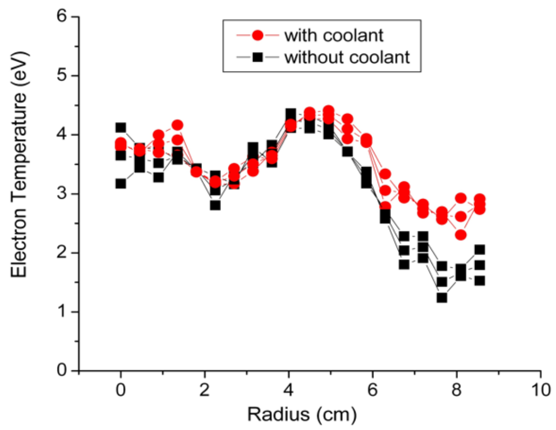

Fig. 7. Electron temperature (at 4 kW in argon) with and without the DI water coolant in the source. The scatter in the plots are from experiments done on 3 different days.

Having confirmed this crucial step, henceforth we always performed experiments in PISCES-RF with the DI water coolant flowing through the ceramic cylinders. This allowed us to safely increase the RF power to the helicon antenna and start producing steady state plasmas at much higher powers. Ramping up the RF power capability allowed us to be able to generate high density plasma in hydrogen, as will be shown in the later sections.

4.2 Plasma heating and steady state temperature distributions on the plasma facing ceramic surface

We used IR imaging to investigate the thermal issues of the plasma facing inner ceramic surface, for steady state operations of the helicon source at RF powers of up to 20 kW. Strategically placed IR cameras allowed measurements of the spatio-temporal variation of the temperatures of the inner plasma facing ceramic surface. The IR camera gave two important pieces of information. We can calculate the effective heat deposited by the plasma on the inner ceramic. When this heat from the plasma is effectively removed by the DI water coolant, the system comes to thermal equilibrium within some characteristic time scale. This gives the final steady state temperature of the inner ceramic surface.

The temperature, at each pixel, is measured as a function of time: *T(t)*. To calculate the effective heat deposited on the inner ceramic surface, we use the theory of transient heat conduction through a semi-infinite solid [42]. The plasma turns on in less than a second and acts as a source of a constant heat flux on any point on the inner ceramic surface. Near the beginning of this constant heat flux, when the heat front has not yet had the time to reach the outer cooled surface of the ceramic, the approximation of a semi-infinite solid is valid. Since bodies of finite thickness can be treated as infinitely wide at the beginning of a constant heat pulse, the analytical solutions for this case can be applied (see section 2.3.3.1 of Ref. 42). In that case, the temperature as a function of time, at each point on the inner ceramic surface, is given by

$$T(t) = T_0 + \left(\frac{2}{\sqrt{\pi}}\right).\left(\frac{\dot{Q}_0}{b}\right).\sqrt{t} \tag{4}$$

where $T(t)$ is the instantaneous temperature, T_0 is the initial temperature, $\dot{Q}_0$ is the constant heat flux and b is a constant which is determined by the thermal properties of the ceramic itself. Denoting ρ as the density, λ as the thermal conductivity and C_p as the specific heat of the material at constant pressure, we have $b^2 = \rho\lambda C_p$. Rearranging and squaring equation (4), we get

$$[T(t) - T_0]^2 = K.t \tag{5}$$

which is effectively a straight line with slope *K*. Thus, from the experimentally measured slope *K* and using the known material constants to calculate *b*, we can infer the heat flux on each point (experimentally, for each pixel on the IR camera screen that corresponds to a point on the ceramic) of the inner plasma facing ceramic surface from the expression:

$$\dot{Q}_0 = \left(\frac{\sqrt{\pi}}{2}\right).b.\sqrt{K}. \tag{6}$$

Finally, taking such inferred values of the heat flux from each pixel of each of the IR camera positions, we can construct the $z - \theta$ maps of the heat fluxes (for example, see Fig. 8). This is shown for 10 kW of RF power in argon plasma and a DI water coolant flow rate of ~ 22 GPM, in a magnetic field geometry where the plasma directly contacts the middle of the ceramic, near z = 0 (the worst possible scenario). In Fig. 8, we also show the footprint of the m = 1 RF antenna when unraveled and plotted on the $z - \theta$ plane. It is clearly seen that the largest heat deposition is under the straps of the helicon antenna, connected to the live, non-grounded, side of the RF power supply. When integrated over the total surface of the cylinder, the total heat deposited is ~ 1.68 kW, which is 16.8 % of the net input RF power. From similar analysis for several RF powers (1.5 – 10 kW in argon plasma), we find that the heat deposition increased linearly with RF power (as shown in Fig. 17).

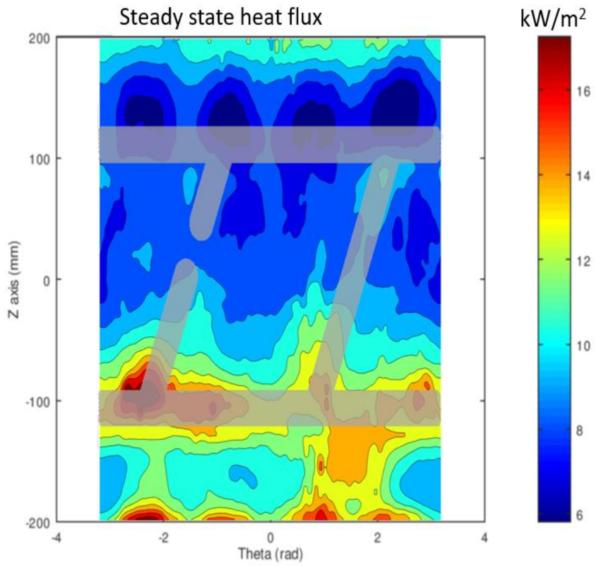

Fig. 8. The inferred 10 kW argon plasma heat flux on the plasma facing inner ceramic surface, along with the footprint of the helicon antenna superimposed (in semi-transparent, light gray).

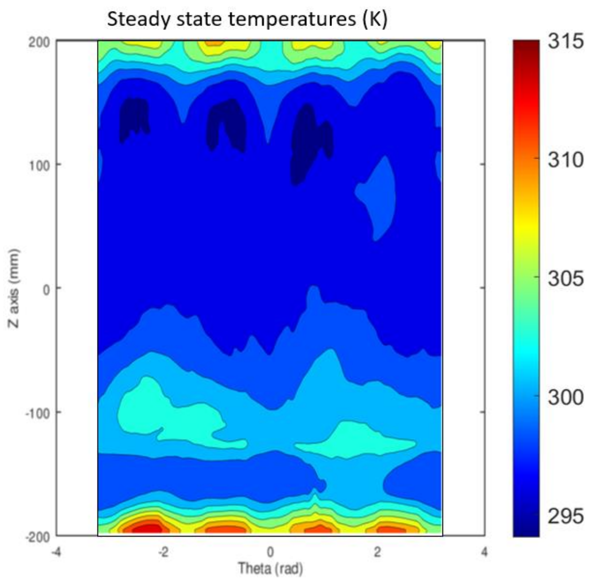

Fig. 9. Steady state temperature distribution due to 10 kW argon plasma on the plasma facing inner ceramic surface.

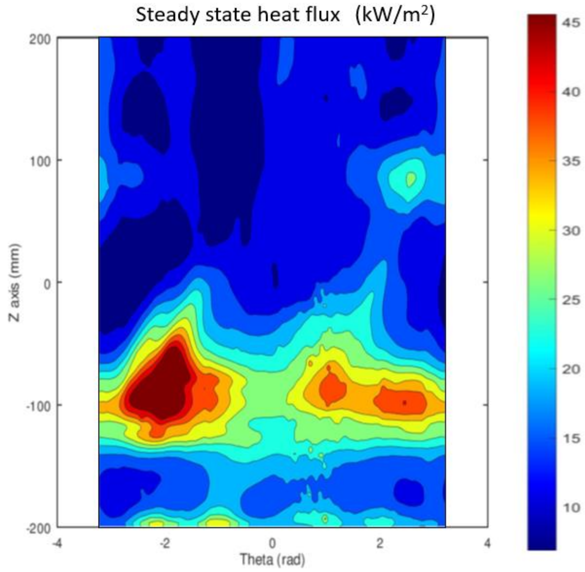

Fig. 10. The inferred 10 kW hydrogen plasma heat flux on the plasma facing inner ceramic surface.

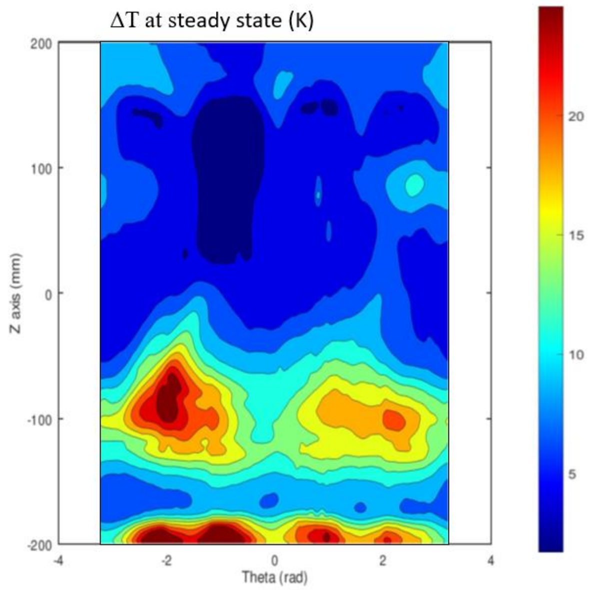

Fig. 11. Steady state spatial distribution of the temperature increase, with respect to the initial values, at 10 kW of hydrogen plasma.

In Fig. 9, we show the spatial pattern of the steady state temperatures on the plasma facing inner surface of the ceramic, for 10 kW argon plasma. Before the plasma was turned on, the ceramic was kept at a uniform surface temperature of 293 K. The DI water coolant can remove most of the heat as the ceramic surface does not get very hot. The hottest portions of the ceramic are at the very ends. This is due to the constraints of the ceramic-metal brazing technique where ~ 1.5 cm of the edges of the ceramic are not directly in contact with the DI water coolant. We find that the regions under the helicon antenna strap remain colder even though they have the maximum heat deposited under them, thus signifying the effectiveness of the DI water coolant in removing the heat. Moreover, as mentioned earlier, the separation between the two magnets (as shown in Fig. 2) near the helicon antenna allows the magnetic field lines under the ceramic to bulge out. Thus, the plasma hits the ceramic at z = 0 which we envision to be the worst-case scenario for the MPEX source. Even then, we see that the maximum heating is under the straps of the helicon antenna and not at the spatial location where the plasma is supposed to hit the inner surface of the ceramic.

Fig. 10 shows the final $z - \theta$ map of the steady state heat flux for 10 kW of hydrogen plasma and a DI water coolant flow rate of ~ 22 GPM. The magnetic field profile is the same as used in argon, but the magnitude is much lower (~ 200 G) in order to ensure proper RF matching. Again, it is clearly seen that the largest heat deposition is under the straps of the helicon antenna, connected to the live (non-grounded) side of the RF power supply. From similar analysis for several RF powers (2 – 20 kW), we find that the heat deposition increases linearly with RF power. When integrated over the total surface of the cylinder, the total heat deposited is ~ 2.76 kW, which is 27.6% of the net input RF power. Thus, we find that the net heat deposited from the plasma is higher in case of hydrogen plasma when compared to argon plasma.

In Fig. 11, we see the spatial pattern of the increase in the temperatures on the inner surface of the ceramic with respect to the initial uniform temperature before the plasma was turned on. This data is for 10 kW of steady state hydrogen plasma. The ceramic was at a uniform surface temperature of 293 K, before the plasma was turned on, and the hottest parts of the ceramic are ~ 25 K higher for steady state operating conditions. Again, we find that even though there is considerable heat deposition right under the helicon antenna straps (see Fig. 10), the DI water coolant is effective in cooling that area, but the hottest portions of the ceramic are near the very ends, which are not in direct contact with the DI water coolant, due to mechanical constraints of the titanium brazing. Even then, the maximum increase in temperature, for 10 kW of RF power, at steady state conditions is only ~ 25 K, which should not be of much concern in terms of thermal stresses in the ceramic.

4.3 Calorimetry of the DI water coolant

To measure the net heat being removed by the DI water coolant, we used two thermocouples to measure the inlet and the outlet temperatures of the DI water. Knowing the flow rate of the DI water coolant, and measuring the temperature difference, we have the net heat (Q), given by

$$Q = m.\ C.\ \Delta T \qquad (7)$$

where m is the mass of DI water coolant flowing per unit time, C is the specific heat capacity of DI water and ΔT is the measured temperature difference. Since we had to take the difference of two large numbers to get a very small value, these measurements were prone to many errors. The thermocouples are extremely sensitive to RF noise, hence we had to ensure proper RF shielding of the cables with proper grounding to reduce RF pickup.

Moreover, for relatively low RF powers, if we used the standard ~ 22 GPM of flow that was accessible to us using the recirculating chiller, the increase in the DI water temperature was of the same order of the noise, hence we had to add another valve to reduce the flow to the lowest possible value, which in our case was ~ 2 GPM. For such low flow rates, the measured temperature differential was above the noise. Fig. 12 gives an example of such measurements, for relatively low RF powers, in high density argon helicon plasma. We see that as we increase the RF power, the steady state saturated value of the temperature differential also increases, which is consistent with expectations. Moreover, we also get an estimate of the time that the system takes to come to thermal equilibrium. For 2 GPM of flow, it takes ~ 2 minutes to reach the steady state. Using the data in Fig. 12 and equation (7), we find that the net heat removed by the DI water for 3 kW, 4 kW and 5 kW, is 756 W (25.2%), 972 W (24.3%) and 1134 W (22.7 %) respectively.

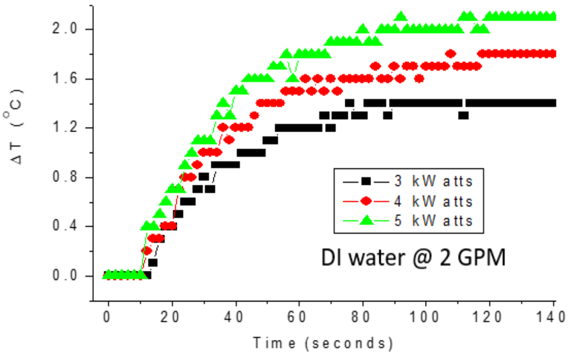

Fig. 12. Temperature difference between the outlet and the inlet of the coolant as a function of time.

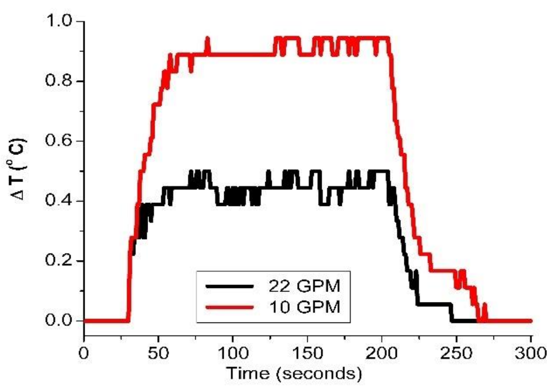

Fig. 13. Temperature difference between the outlet and the inlet of the coolant (DI water) as a function of time, at 10 kW of input RF power for argon plasma, shown for flow rates of 10 GPM and 22 GPM, showing consistency of the calorimetry method.

In Fig. 13, we show another example of thermocouple data, but for higher powers in argon plasma. For 10 kW of input RF power the DI water coolant had to remove a much larger amount of heat, and hence we could obtain decent signal to noise ratio even at higher flow rates of the DI water coolant. Here we also show the consistency in the net heat removed by changing the flow rates of the DI water coolant for the same RF power plasma. For example, for 10 kW argon plasma operation, calorimetry at 10 GPM yields a net heat removal of 2.48 kW (24.8%) and for a flow rate of 22 GPM, we get 2.64 kW (26.4%). We also notice that as we increase the flow rate, the time it takes to reach steady state levels decrease, as expected. For ~ 10 GPM, it takes ~ 1 minute and for ~ 22 GPM (the maximum flow rate for the recirculating chiller we are using), it takes ~ 30 secs to reach saturation. Moreover, even for steady state conditions, the increase in the temperature of the DI water coolant is nominal (< 1 C) which confirms the effectiveness of the cooling method.

4.4 High density plasma production

In this section, we show some radial profiles of plasma density for both argon and hydrogen plasmas for steady state conditions. The density is measured at two ports situated at 0.8 m and 1.5 m downstream of the RF helicon source (see Fig. 1). In, Fig. 14, we show a power scan in the range of 5 – 10 kW of RF power. The peak density at r = 0 is reached at ~ 5 to 6 kW of RF power input. The peak densities reach ~ 2.5 x 10^{19} m^{-3}. This is also consistent with the data shown in Fig. 6. In the helicon mode, for increasing RF powers, the peak density at one axial location initially increase with power, but then can saturate and even drop [43]. This phenomenon is attributed to neutral depletion near the center of the plasma due to very strong ionization in the helicon mode.

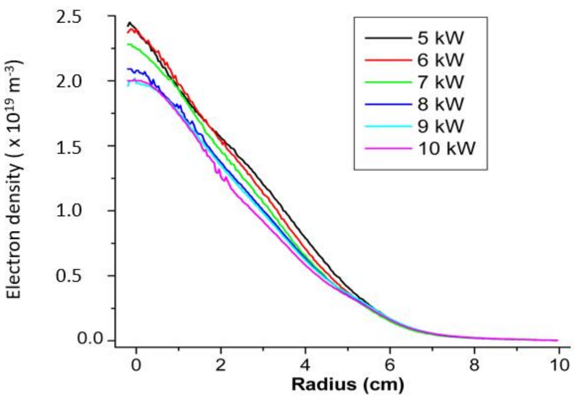

Fig. 14. Radial profiles of argon plasma density measured 0.8 m downstream of the RF helicon source.

In Fig. 15 and Fig. 16, we show the radial profiles of the plasma density for steady state hydrogen plasma, measured 0.8 m and 1.5 m downstream of the RF helicon source, respectively. The source was operated with ~ 6 mTorr of neutral hydrogen gas flowing at 100 sccm and with uniform magnetic field of 200 G. Helicon sources have windows of operation in the operating parameter space (flow, pressure, magnetic field and RF power), and we found that this combination allowed us to go into the helicon mode. From both the plots, we find that the helicon mode is achieved at ~ 8 kW in our device. The plasma density at r = 0 is ~ 10^{17} m^{-3} for up to 7 kW and jumps to ~ 0.3 x 10^{19} m^{-3} at 8 kW and increases thereafter. A sudden discrete jump of more than an order of magnitude in the plasma density, as a function of RF power or magnetic field, along with centrally peaked density profiles, is the standard signature of the development of the helicon core mode [12 – 17].

For 20 kW in hydrogen, we achieve peak central plasma densities of ~ 1.35 x 10^{19} m^{-3} at the port 0.8 m downstream of the helicon source. From Fig. 16, we see that even 1.5 m downstream of the plasma source, the peak central densities are ~ 1 x 10^{19} m^{-3}, which makes this device PMI relevant. Moreover, even at 20 kW of steady state operation, the increase in the DI water temperature is only slightly more than 1 C (at DI water coolant at a flow rate of 22 GPM). Thus, it is possible to operate PISCES-RF in steady state and increase the total fluence.

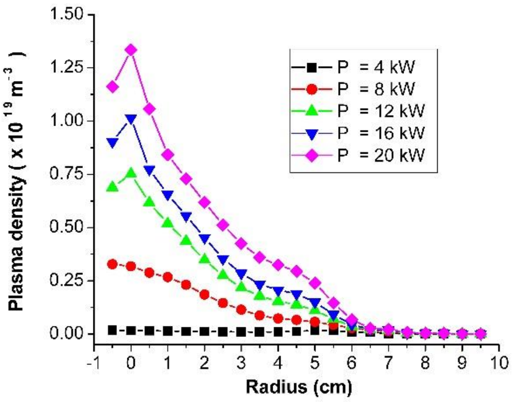

Fig. 15. Radial profiles of hydrogen plasma density measured 0.8 m downstream of the RF helicon source.

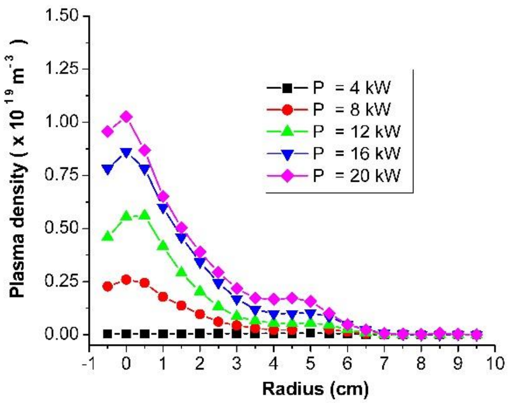

Fig. 16. Radial profiles of hydrogen plasma density measured 1.5 m downstream of the RF helicon source. Note: the ranges of the axes are kept identical to Fig. 15.

In Figs. 17 and 18, we show the effect of increasing RF power on the central hydrogen plasma density measured at the two ports, 0.8 m and 1.5 m downstream of the source. After we achieve the helicon core mode for hydrogen plasma, in the range of the RF powers used in this study (up to 20 kW), the device is still in the linearly increasing regime with forward power and has not reached saturation. On the other hand, the electron temperature seems to have reached saturation (~ 8 eV at 0.8 m and ~ 3 eV about 1.5 m away from the RF source) once we have reached the high-density helicon core mode. From the measured ion saturation current, we calculate that the ion fluxes to the probes are ~ 3 x 10^{23} $m^{-2}sec^{-1}$ at 0.8 m and ~ 2 x 10^{23} $m^{-2}sec^{-1}$ at 1.5 m away from the RF source respectively. Note that the measurements shown in Figs. 17 and 18 are taken for one particular set of plasma operating conditions (with ~ 6 mTorr of neutral hydrogen gas flowing at 100 sccm and with uniform magnetic field of 200 G). Plasma source parameter optimization to achieve the highest plasma densities or highest electron temperatures have not yet been done.

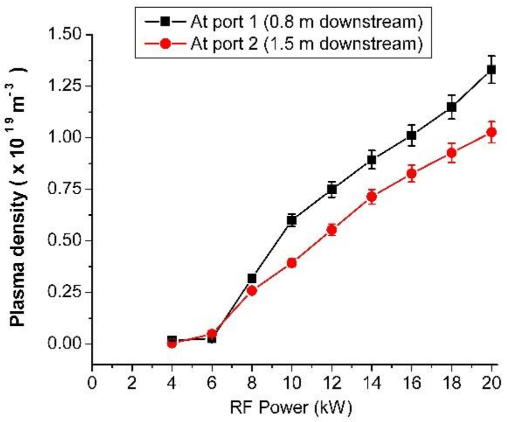

Fig. 17. Hydrogen plasma density vs. RF power measured at 0.8 m and 1.5 m downstream of the RF helicon source.

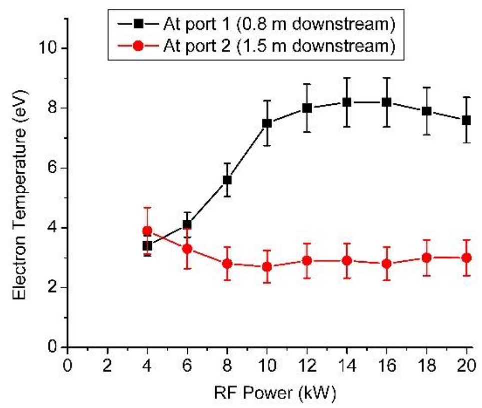

Fig. 18. Electron temperature vs. RF power measured at 0.8 m and 1.5 m downstream of the RF helicon source.

4. Discussions

We have successfully produced high density (n > 10^{19} m^{-3}) argon and hydrogen helicon plasmas in steady state using a novel RF source design where the RF transparent window is completely immersed in a blanket of coolant (DI water in this case). In the process, we have studied different aspects of this source including RF absorption by the DI water coolant, spatiotemporal measurements of the heat deposited by the plasma and steady state temperature distributions on the inner plasma facing ceramic layer and finally the net heat that has to be removed for safe long-term operation of the device. We ensured that PMI relevant plasmas can be generated in this device in steady state. This work also lays the basis of characterization of the source assembly design for much higher power helicon devices being designed at ORNL. While achieving our goal of producing high density hydrogen plasma in steady state, we also learnt several things along the way.

We have measured the net heat removed by the DI water coolant have identified two possible physics mechanisms contributing to the heating of the DI water coolant: the plasma heat deposited on the plasma facing inner ceramic and absorption of a fraction of the RF in the coolant. We found that for argon, approximately 16 – 19% of the net RF input power gets deposited on the inner ceramic layer directly due to the plasma hitting the ceramic. In addition to this, studies of the effect of the DI water coolant on the RF matching network with a VNA and Pearson transformer have shown that ~ 8 – 11% of the RF power is directly absorbed by the DI water coolant. Now, from calorimetry, using independent measurements of the inlet and outlet DI water temperatures, we find that ~ 25 – 30% of the input RF heat load being removed by the DI water coolant. Thus, the three independent thermal measurements of the different aspects of the antenna assembly seems to be consistent with each other, across a wide range of RF power. We present them in Fig. 19. The black squares represent the RF absorption due to the effect of the DI water in between the two ceramic cylinders. The red circles are calculated from the IR camera data, using the equations 4 – 6, which represent how much the plasma heat is deposited on the ceramic which in turn is transferred to the DI water coolant. The sum of the two sources of heat input to the DI water coolant is shown in magenta inverted triangles. Completely independently, we plot the measured heat removed by the DI water coolant from calorimetry, as blue triangles. Within measurement errors, they seem consistent over the whole range of 1.5 – 10 kW for argon plasma. Straight lines, going through the origin, fit to the data in Fig. 19 give slopes of 0.18 for the heat deposited on the plasma facing ceramic as measured by the IR camera, 0.09 for the RF absorption and 0.26 as measured by calorimetry.

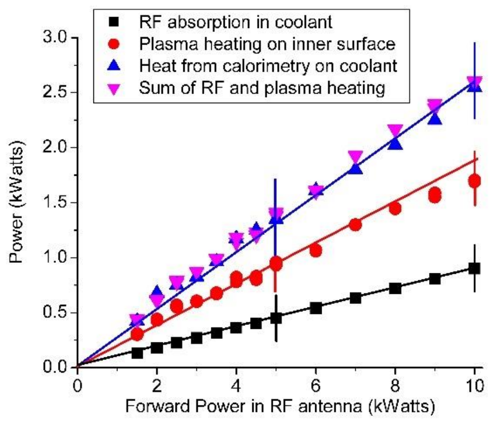

Fig. 19. Consistency amongst thermal measurements in argon plasmas up to 10 kW.

For hydrogen plasma, we find that the heat deposition by the plasma on to the inner ceramic is 25 –

29% and from calorimetry the net heat removal is 35 – 40 %. Taking the RF absorption to be 7 – 11 %, we find consistency for hydrogen plasmas too. This is plotted in the Fig. 20. Here also we find that the thermal measurements are linearly increasing with RF power. Straight lines, going through the origin, fit to the data in Fig. 20 give slopes of 0.28 for the heat deposited on the plasma facing ceramic, as measured by the IR camera, 0.09 for the RF absorption and 0.36 as measured by calorimetry. Recent work done on the device Proto-MPEX at ORNL also shows ~ 40 % of heat being deposited on the RF transparent window [REF. 47 needed], which seems to be consistent with our finding.

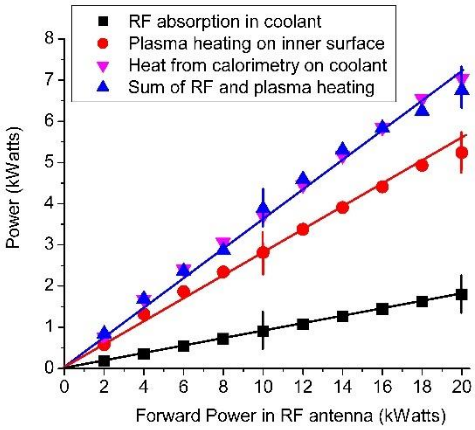

Fig. 20. Consistency amongst thermal measurements in hydrogen plasmas up to 20 kW.

We would like to clarify that in this paper we concentrated on studying the actively cooled RF transparent window design to verify all the RF and thermal issues and to check whether they are suitable as sources for PMI devices. In addition, one has to note that helicon sources have very strict windows of operation, in terms of the source parameters such as external magnetic field profile and magnitude near the antenna, gas flow, neutral gas pressure etc. These operating windows also depend on the gas being used and are very narrow for hydrogen, which is the most difficult gas to work with in terms of RF plasma generation in the helicon mode [44 – 46]. We have not yet tried to optimize the high-density plasma production in this paper by playing with the windows of operation. We have just ensured that we could find some set of source parameters, for both argon and hydrogen so as to achieve the helicon mode of operation, as that gives the high densities that these helicon sources are famous for. Optimization of the external source parameters for the highest possible densities and investigating the windows of operation for various fusion relevant gases such as helium, deuterium and hydrogen remain a task for the near future. We had chosen to operate with hydrogen plasma, as being the lightest gas, it is the most difficult to produce the highest densities with and it also has the smallest windows of operation to be in the helicon mode [45 – 46].

In addition to developing and studying the DI water cooled source for future PMI experiments in the PISCES-RF device, we are also using results from these experiments as a source design test for MPEX. The Materials Plasma Exposure eXperiment (MPEX) is planned to be a world leading linear plasma facility to expose neutron irradiated samples to high ion fluences (10^{31} m^{-2}) in order to examine the multivariate PMI effects that will be present in next step fusion devices [3 – 4]. High power (200 kW) will be coupled through an RF transparent window at a frequency of 13.56 MHz. This very high-power RF concept has been demonstrated on the proto-MPEX experiment for short pulses with an uncooled antenna [23 – 24].

In conclusion, we have designed an actively cooled helicon antenna with a water-cooled window for steady state plasma operation, and also for possible use in the MPEX linear plasma device. The prototype has been built and tested in the steady-state up to 20 kW at UCSD. We have ensured high density plasma production in both argon and hydrogen, by achieving the helicon plasma mode of operation, even with the DI-water coolant flowing in between the ceramic layers. We find that at 20 kW of RF power, we can achieve > 10^{19} m^{-3} in hydrogen plasma and an ion flux of ~ 2 x 10^{23} $m^{-2}sec^{-1}$ even 1.5 m away from the RF source. For these conditions, in the steady state, the increase in the DI-water coolant temperature is ~ 1C, which is nominal. It took ~ 30 secs for the DI water coolant to come to saturation. We have also measured the spatial variations in the final steady state temperature of the inner plasma facing ceramic surface, which will determine the unequal expansions of neighboring regions of the ceramic from which the stresses can be calculated. In addition, the spatial variation of the deposited heat can also be used as an input parameter to numerical modelling studies. For argon plasma, from the IR camera measurements, the net heat flux integrated over the whole inner ceramic, is given by a scaling law: $\dot{Q}_0 \sim 0.168 * RF\ Power$ (in kW). Similarly, for hydrogen helicon plasma, the scaling law would be given by $\dot{Q}_0 \sim 0.284 * RF\ Power$ (in kW). Understanding these trends are important when trying to extrapolate thermal test results from PISCES-RF to other devices being planned. These experimental results have been correlated to thermal-hydraulic (CFD) and thermal-structural (FE) simulation and are being extrapolated to 200 kW [26]. Thus, we can say that in addition to understanding the thermal properties of this novel liquid cooled RF helicon source and ensuring high density steady state plasma operation with fusion relevant gases, the results from our experiments are also helping in designing the source of next generation PMI devices.

Acknowledgments

This research is sponsored by the Office of Fusion Energy Sciences, U.S. Department of Energy, under contract DE-FG02-07ER54912. The authors also want to thank Mr. Leopoldo Chousal and Mr. Tyler Lynch for their help in technical details on mechanical issues.

References

[1] J. Linke, et al., Challenges for plasma-facing components in nuclear fusion, Matter and Radiation at Extremes **4**, 056201 (2019)

[2] Ch. Linsmeier et al., Material testing facilities and programs for plasma-facing components testing, Nuclear Fusion **57**, 092012 (2017)

[3] J. Rapp, The Challenges of Plasma Material Interactions in Nuclear Fusion Devices and Potential Solutions, 72 (2017) 211-221.

[4] J. Rapp et al, The Development of the Plasma-Material Interaction Facilities for the Future of Fusion Technology, Fusion Science and Technology, 64 (2013) 237-244.

[5] D. Naujoks, G. Fussmann and H. Meyer, Contributions to Plasma Physics **38,** 127 (1998)

[6] Goebel D.M., Campbell G. and Conn R.W., Journal of Nuclear Materials **121,** 277 (1984)

[7] Y. Hirooka et. al., Journal of Vacuum Science and Technology A **8,** 1790 (1990)

[8] N. Ohno et. al., Nuclear Fusion **41,** 1055 (2011)

[9] M. Shimada, C.N. Taylor, R.J. Pawelko, L.C. Cadwallader, and B.J. Merrill, Tritium Plasma Experiment Upgrade and Improvement of Surface Diagnostic Capabilities at STAR Facility for Enhancing Tritium and Nuclear PMI Sciences, Fusion Science and Technology **71**, 310-315 (2017)

[10] G. J. van Rooij et. al., Applied Physics Letters **90,** 121501 (2007)

[11] De Temmerman G. et. al., Fusion Engineering Design **88,** 483 (2013)

[12] R. W. Boswell and F. F. Chen, "Helicons – the early years," IEEE Transactions on Plasma Science **25**, 1229 (1997)

[13] F. F. Chen and R. W. Boswell, "Helicons – the past decade," IEEE Transactions on Plasma Science **25**,1245 (1997)

[14] F. F. Chen, "Helicon discharges and sources: a review," Plasma Sources Science and Technology **24**, 014001 (2015)

[15] S. Shinohara, Helicon high-density plasma sources: physics and applications, Advances in Physics: X, **3: 1**, 1420424, (2018)

[16] C. M. Franck, O. Grulke and T. Klinger, Physics of Plasmas **10,** 323 (2003)

[17] S. C. Thakur, C. Brandt, L. Cui, J. J. Gosselin, A. D. Light, and G. R. Tynan, Multi-instability plasma dynamics during the route to fully developed turbulence in a helicon plasma, Plasma Sources Science and Technology, Plasma Sources Sci. Technol. **23**, 044006 (2014).

[18] Y. Mori et al., "High density hydrogen helicon plasma in a non-uniform magnetic field," Plasma Sources Science and Technology **13**, 424 (2004)

[19] J. P. Squire et al., "High power light gas helicon plasma source for VASIMR," Thin Solid Films **579**, 506-507 (2006)

[20] B. D. Blackwell et al., "Design and characterization of the Magnetized Plasma Interaction Experiment (MAGPIE): A new source for plasma-material interactions studies," Plasma Sources Science and Technology **21**, 055033 (2012)

[21] J. Rapp et al., Latest Results from Proto-MPEX and the Future Plans for MPEX, Fusion Science and Technology **75: 7**, 654, (2019)

[22] I. Furno, Helicon wave-generated plasmas for negative ion beams for fusion, EPJ Web of Conferences **157**, 03014 (2017)

[23] J. Rapp et al., The Development of the Material Plasma Exposure eXperiment MPEX, IEEE Transactions on Plasma Science **44**, 3456-3464 (2016)

[24] J. Rapp et al., Developing the Science and Technology for the Material Plasma Exposure eXperiment, Nuclear Fusion **57**, 116001 (2017)

[25] A. Lumsdaine, et al., Design and Analysis of an Actively Cooled Window for a High Power Helicon Plasma Source, IEEE Transactions on Plasma Science, submitted (2019)

[26] A. Lumsdaine, et al., Testing and Analysis of Steady-State Helicon Plasma Source for the Material Plasma Exposure eXperiment (MPEX), ISFNT (2019)

[27] M. Burin, G. R. Tynan, G. Y. Antar, N. A. Crocker, and C. Holland, On the transition to drift turbulence in a magnetized plasma column, Physics of Plasmas 12, (2005), 052320

[28] C. Holland, et al., Observation of Turbulent-Driven Shear Flow in a Cylindrical Laboratory Plasma Device, Physical Review Letters, 96 (2006), 195002

[29] Z. Yan, et al., Intrinsic Rotation from a Residual Stress at the Boundary of a Cylindrical Laboratory Plasma, Physical Review Letters, 104 (2010), 065002

[30] M. Xu, et al., Generation of a Sheared Plasma Rotation by Emission, Propagation and Absorption of Drift Wave Packets, Physical Review Letters, 107, (2011), 055003

[31] P. Manz, at al, Nonlinear energy transfer during the transition to drift-interchange turbulence, Plasma Physics and Controlled Fusion, 53, (2011), 095001

[32] S. C. Thakur, et. al., Suppression of drift wave turbulence and zonal flow formation by changing axial boundary conditions in a cylindrical magnetized plasma device, Physics of Plasmas, 20, (2013), 012304

[33] L. Cui, et al., Spontaneous profile self-organization in a simple realization of drift-wave turbulence, Physics of Plasmas, 23, (2016), 055704

[34] S. C. Thakur, et. al., Development of core ion temperature gradients and edge sheared flows in a helicon plasma device investigated by laser induced fluorescence measurements, Physics of Plasmas, 23 (2016), 082112

[35] R. Hong, et al., Tracing the pathway from drift wave turbulence with broken symmetry to the production of sheared axial mean flow, Physical Review Letters, 120, (2018), 205001

[36] P. Manz, et al., Plasma Blob Generation due to Cooperative Elliptic Instability, Physical Review Letters, 107, (2011), 195004

[37] C. Brandt, et al., Spatiotemporal Splitting of Global Eigenmodes due to Cross-Field Coupling via Vortex Dynamics in Drift Wave Turbulence, Physical Review Letters, 113, (2014), 265001

[38] S. C. Thakur, et al., Formation of the Blue Core in Argon Helicon Plasma, IEEE Transactions on Plasma Science, 43, 8, (2015), 2754

[39] S. C. Thakur, et. al., Laser induced fluorescence measurements of ion velocity and temperature of drift turbulence driven sheared plasma flow in a linear helicon plasma device, Physics of Plasmas, 19, (2012), 082102

[40] J. F. Caneses et. al., Differential pumping requirements for the light-ion helicon source and heating systems of Proto-MPEX, Phys. Plasmas **25**, 083518 (2018)

[41] S. C. Thakur, M. Simmonds et. al., Infrared Imaging technique for thermal studies of the plasma facing ceramic surface of a helicon plasma source, *in preparation (2020)*

[42] H. D. Baehr and K. Stephan, Heat and Mass Transfer, Springer-Verlag Publications (1998)

[43] C. Mark Denning, M. Wiebald and J. E. Scharer,

Observations of neutral depletion and plasma acceleration in a flowing high-power argon helicon plasma, Physics of Plasmas **15,** 072115 (2008)
[44] A. J. Perry, D. Vender, and R. W. Boswell, The application of the helicon source to plasma processing, Journal of Vacuum Science & Technology B, 9, 310 (1991)
[45] Y. Sakawa, T. Takino and T. Shoji, Contribution of slow waves on production of high-density plasmas by m50 helicon waves, Physics of Plasmas **6**, 4759 (1999)
[46] M. Light, F. F. Chen and P. L. Colestock, Low frequency electrostatic instability in a helicon plasma, Physics of Plasmas 8, 4675 (2001)
[47] Ref. for heat deposition on Proto-MPEX ceramic.